


3D milling modeling: mechanical actions, strains, strain rates and temperature calculations in the three cutting zones

Wadii Yousfi¹ · Olivier Cahuc¹ · Raynald Laheurte¹  · Philippe Darnis¹ · Madalina Calamaz²

Received: 28 August 2017 / Accepted: 8 November 2017 / Published online: 17 November 2017
© Springer-Verlag London Ltd., part of Springer Nature 2017

Abstract Analytical and semi-analytical modelling of manufacturing processes involving material removal are of great interest to scientists and industrialists. With this type of modelling, we are able to identify optimal cutting parameters based on geometric and thermomechanical quantities, without having to carry out experimental trials or costly simulations (thus saving time and reducing costs). Compared with other machining techniques, milling involves additional complexities arising from the variation in geometric parameters in the machining configuration and in kinematic parameters when operational. This paper presents a new 3D modelling analysis applied to milling, which takes into account phenomena generated by the three-dimensional kinematics of the process. To complete this thermomechanical approach to cutting, improvements have been made to a basic model configuration. The model that has been developed can now map strains, strain rates, stresses and temperatures along the cutting edge, in the primary, secondary and tertiary shear zones. Forces and cutting moments at the theoretical tool tip are estimated at a local then a global scale, and compared with experimental results from previous work.

Keywords Milling · Strain gradients · Strain rate gradients · Cutting action torsor · Cutting moment

✉ Wadii Yousfi
wadiiyousfi@yahoo.fr

¹ University of Bordeaux, I2M UMR 5295, 351 cours de la Libération, 33400 Talence, France

² Arts et Métiers ParisTech, I2M UMR 5295, 351 cours de la Libération, 33400 Talence, France

Nomenclature

x_c, y_c	Coordinates of a point in the secondary shear zone.
a_p'	Apparent depth of cut ($m.min^{-1}$).
d_a	depth of plastic deformation zone (mm).
f	Feed rate (mm).
f_z	Tooth feed rate ($mm.tooth^{-1}$).
r_a	Cutting edge radius (mm).
r_β	Tool nose radius (mm).
α_0	Clearance angle ($^\circ$).
ϕ	Shear angle ($^\circ$).
γ_0	Rake angle ($^\circ$).
$\delta.t_2$	Thickness of shear band in the secondary shear zone (mm).
$\alpha.l_c$	Length of shear contact along rake face (mm).
P_{s1}, P_{s2}	Surface power density above and below stagnation point ($W.m^{-2}$).
$\sigma_{eq,S'_1}, \sigma_{eq,S'_2}$	Equivalent stress above and below stagnation point (MPa).
$\dot{\varepsilon}_{eq,S'_1}, \dot{\varepsilon}_{eq,S'_2}$	Overall strain rate above and below stagnation point (s^{-1}).
$h_m(\theta_1), h_m(\theta_2)$	Instantaneous cutting feed for two angle positions θ_1 and θ_2 (mm).
ΔT	Temperature difference ($^\circ C$).
T_{SSZ}	Temperature in the secondary shear zone ($^\circ C$).
V_{chip}	Chip speed along to cutting edge ($m.s^{-1}$).
V_c	Cutting speed ($m.min^{-1}$).
V_g	Sliding speed of the chip along to cutting edge ($m.s^{-1}$).
V_S	Sliding speed in the primary shear zone ($m.s^{-1}$).
V_t	Speed of material perpendicular to cutting edge ($m.s^{-1}$).

V_z	Speed of material parallel to cutting edge ($m.s^{-1}$).
K_{th}	Thermal conductivity ($W.m^{-1}.^{\circ}C^{-1}$).
a	Thermal diffusivity ($m^2.s^{-1}$).
dl_i	Elementary length of heat source (m).
R_i and R'_i	Distance between point M and primary heat source and image respectively.
ϕ'_2	Density of heat flux ($W.m^{-2}$).

1 Introduction

This study is based on previous 3D cutting modeling for turning [1–3], drilling [4] and milling [5] processes. The proposed modeling corresponds to an established sectional machining configuration and generating a continuous chip of a ductile steel part.

For the turning configuration, the thermomechanical quantities (strains, strain rates, temperatures and stresses) with a realistic consideration of the cutting edge radius and the tool nose radius [3] have been determined by Toulouse [1] and Laheurte [2] in order to determine all the cutting actions (forces and moments). The definition of the thermal cutting phenomena has been improved by Puigsegur [6]. In the drilling configuration, a semi-analytical approach for the modeling of cutting actions in the case of drilling has been developed by Dargnat [4]. Comparatively to Zhang's work [7], the geometrical defects of the tool, the positioning and orientation defects with respect to the spindle have been integrated, which makes it possible to determine the radial force regarding the forces measured experimentally. In the milling configuration, the torsor of cutting actions at the tip of the tool using an experimental approach to highlight the presence and importance of the cutting moments have been determined by Albert [5] similarly to Wojciechowski [8]. This approach has been extended by Wojciechowski [9, 10] to the study of the influence of the tool cutting edge radius on the cutting forces.

Karagüzel's recent work [11] deals with analytical modeling of combined turning and milling processes by determining instantaneous feed in three configurations: orthogonal, tangential and coaxial. The specific forces (cutting, tangential and parallel to the tool's axis) for each elementary length of the cutting edge are a function of the instantaneous feed which depends on the position along the cutting edge and the specific pressures.

Based on the Engin's works [13], Kaymakci [12] define the kinematics of a straight-edge tool oriented in the turning space. The cutting forces are determined in oblique cutting configuration according to the specific cutting pressures. In these works, the kinematics along the cutting edge is not discretized and the contribution of the kinematics on the inter-volumic interactions along the edge is not taken into

account. The additional movements of the chip generated by the geometry and the kinematics are not taken into account either.

For micro-milling application, Kang [14] determine the cutting forces according to the instantaneous feed velocity and the normal and tangential cutting specific pressures. The determination of the instantaneous feed is based on the Fourier series, the third dimension is not considered and the effect of the variation of kinematics along the cutting edge is not taken into account. For the same application, Zhou [15] propose a 3D cutting forces model according to the instantaneous feed velocity. The instantaneous feed velocity is determined with an analytical model. These models do not allow to take into account the 3D effect on the cutting actions generating inter-volumic interactions along the edge.

The milling process has a more complex kinematic definition; this work is positioned in the continuity of the 3D models previously discussed. To improve the modeling, the 3D interactions between the volume elements along the cutting edge are determined by a volumic modeling of the strains fields and strain rates in the three main cutting zones. This study is also based on the kinematics and 3D models presented in the previous works [16] and [17].

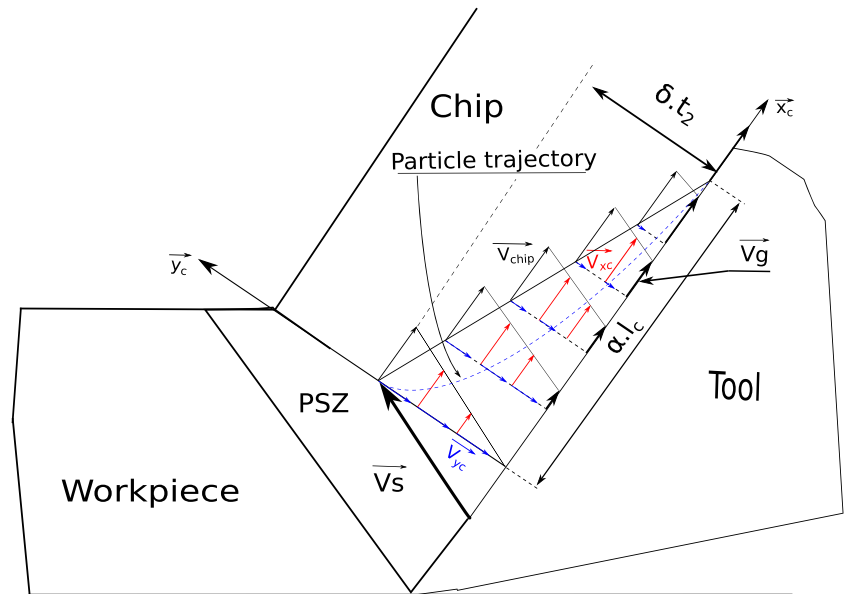
2 Trajectory of a volume element in the shear zones

Along the primary shear zone, the volume element moves from the workpiece towards the chip. The large amount of material displacement generates high strains and strain rates along the thickness of the shear band. A material point passing through the primary shear zone follows a hyperbolic trajectory [4, 18]. The speed component parallel to the shear plane is assumed to be constant. In order to take into account the compression of the material against the rake face, the model considers that each particle entering the secondary shear zone follows a curvilinear trajectory, as shown in (Fig. 1). In fact, along the tool-chip contact surface, the sliding speed V_g is assumed to vary linearly starting with sticky contact close to the tool tip and reaching a speed equal to that of the chip (V_{chip}) [19]. This speed is assumed to vary linearly as a function of V_{chip} with:

$$V_g = \xi \cdot V_{chip}. \quad (1)$$

In order to demonstrate the trajectory of a material point entering the secondary shear zone (taking into account friction at the tool-chip interface), we study a velocity component carried by the \vec{y}_c axis, perpendicular to the cutting surface and varying linearly as a function of x_c . The velocity

Fig. 1 Trajectory of a volume element in the secondary shear zone



component carried by \bar{y}_c is written as a function of a dimensionless coordinate ξ , as follows:

$$V_{y_c}(\xi) = (1 - \xi) \cdot V_s \cdot \cos(\phi - \gamma_0), \tag{2}$$

where V_s is the sliding speed in the primary shear zone.

In the tertiary shear zone, the cross-section of the tool is shown in the calculation scheme as the arc of a circle where the two asymptotes are the clearance face and the rake face (Fig. 2). The tertiary shear zone is described according to the following parameters:

- d_a : depth of plastic deformation zone,
- r_a : cutting edge radius,
- α_0 : clearance angle.

The stagnation point is located where the difference between surface power density on either side of this point is

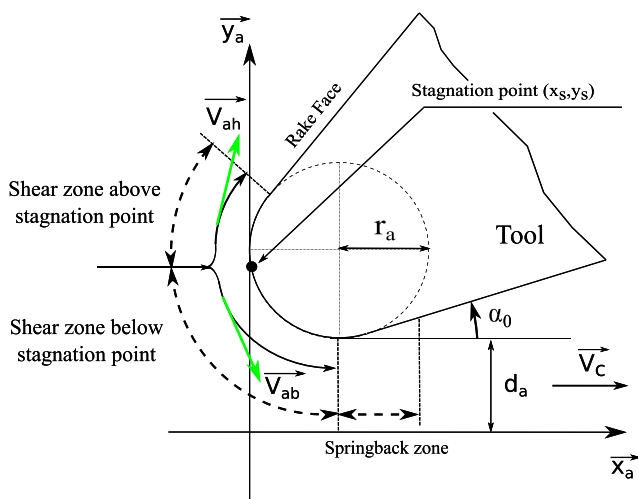


Fig. 2 Trajectory of a volume element in the tertiary shear zone

at its minimum, as shown in (Fig. 3) and the following paragraph. Along the cutting edge radius r_a and for each position S' , the two surface power densities at points S'_1 and S'_2 (middles of the two parts located on either side of this point) are given by

$$P_{s1} = \sigma_{eq,S'_1} \cdot \dot{\epsilon}_{eq,S'_1} \cdot L_1, \tag{3}$$

$$P_{s2} = \sigma_{eq,S'_2} \cdot \dot{\epsilon}_{eq,S'_2} \cdot L_2. \tag{4}$$

The variation in distance L_2 , which determines the position of the stagnation point along the cutting edge radius as a function of the rake angle, is shown in (Fig. 4). Point S'

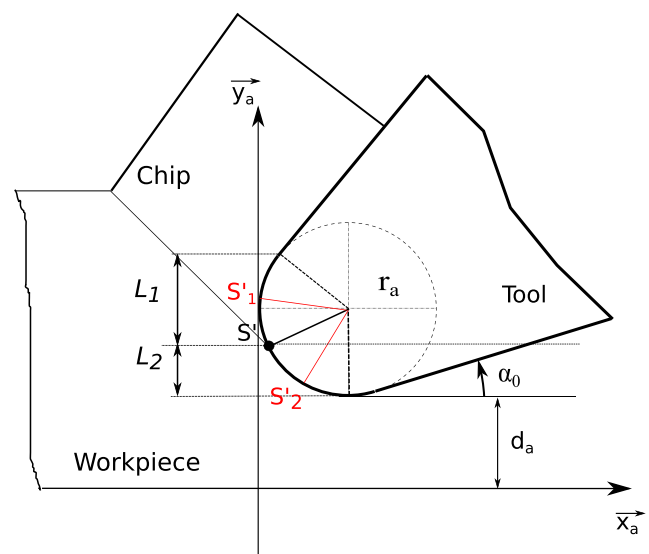


Fig. 3 Positions chosen to calculate surface power density in order to optimize the stagnation point position

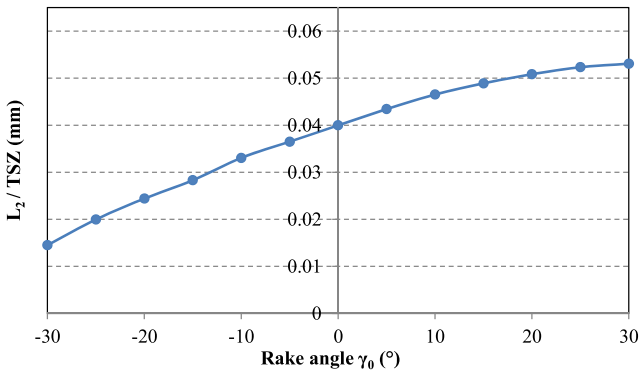


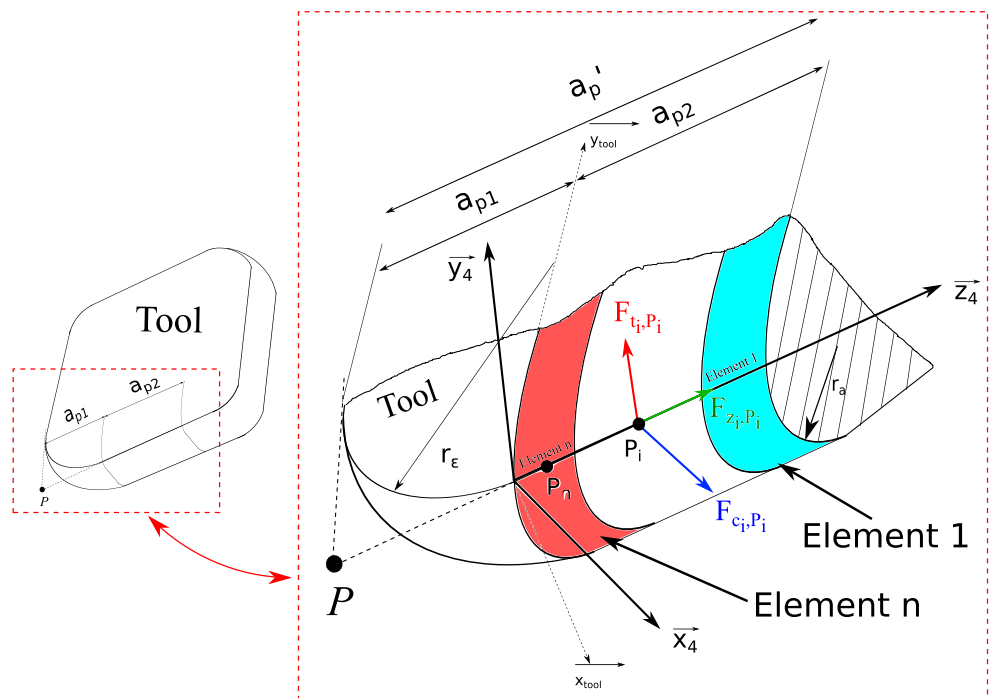
Fig. 4 Variation in stagnation point position as a function of rake angle ($V_c = 60 \text{ m}\cdot\text{min}^{-1}$, $f = 0,2 \text{ mm}$)

moves down the \vec{y}_a axis, passing from positive to negative rake angles.

3 Determining basic cutting actions

Due to the orientation of the tool and the kinematics of the milling process [16], velocity gradients along the cutting edge generate additional chip displacements in all three directions and as a result, they also generate new force components and cutting moments. In this study, we present the overall procedure for calculating macroscopic cutting actions, starting with a detailed description of each characteristic zone. This cutting action torsor is calculated at the tool tip as a function of basic forces along the cutting edge.

Fig. 5 Distribution of forces applied along the cutting edge for a square tool



3.1 Determining strain fields and strain rates in the shear zones

After defining a local coordinate system in each cutting zone, for each direction of the coordinate system, the velocity field is determined as a function of the kinematic and geometric parameters of the cut [17]. Maximum displacements are calculated in the three directions of the cutting zone and the spatial derivative of the displacement field in the shear zones gives the strain tensor. Because of the great strain on the material, the strain rate is not obtained by a time derivative of the strain but by a spatial derivative of the velocity field.

3.2 Study of elementary actions in the case of a square tool

In the case of a square tool insert, two parts of the cutting edge are defined: the first is linear, of length a_{p2} (Fig. 5) and the second is the corner radius, of length a_{p1} . The cutting speed is considered equal to the average of the speeds at the extreme points on each length element (from element 1 to element n).

3.2.1 Study of the linear part of the edge

Along the linear part of the tool and for each length element, changes in strain and strain rate along the edge are determined using the approach proposed by Yousfi [17]. In order to take into account the instantaneous variation in feed

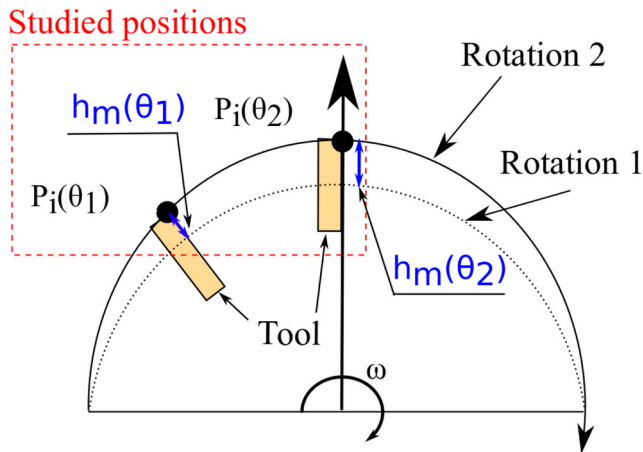


Fig. 6 Tool angle positions studied

$h_m(\theta_i)$ as the tool rotates, two angle positions θ_1 and θ_2 were chosen, corresponding to rotation angles of 135° and 90° , respectively (Fig. 6).

The graphs in Fig. 7a, b show the change in equivalent strain and overall strain rate along the cutting edge in the secondary shear zone (SSZ). For the two angle positions, there is virtually no variation in the equivalent strain along the cutting edge (Fig. 7a) as the depth of cut is equal for all elements. However, the overall strain rate for θ_1 and θ_2 decreases by 6% along the edge (starting with element 1 to element 9).

From the strain and strain rate calculated in the secondary shear zone, the force normal to the rake face in this zone can be calculated from equivalent stress (5) using a Johnson-Cook type of behavior law [20]. This stress is assumed to be equivalent to stress normal to the rake face.

$$\sigma_{eq} = \left(A + B \cdot \varepsilon_{eq}^n \right) \cdot \left(1 + C \cdot \ln \left(\frac{\dot{\varepsilon}_{eq}}{\dot{\varepsilon}_0} \right) \right) \cdot \left(1 - \left(\frac{T_{ave} - T_0}{T_{melt} - T_0} \right)^m \right) \quad (5)$$

where A is the yield strength of the material, B , n are coefficients linked with the work hardening of the material, C is a coefficient of sensitivity to strain rate and m is a coefficient of sensitivity to temperature, T_{melt} is the melting temperature of the material, T_0 the initial temperature of the material. In order to calculate equivalent stress, the average temperature (T_{ave}) in the secondary shear zone is determined from the elementary cutting model using Komanduri and Hou’s approach [21] and incorporating the speed of the corresponding chip into each length element (6).

$$T_{ave}(M) = \frac{\varphi'_2}{\pi \cdot K_{th}} \int_0^{\alpha \cdot l_c} e^{-\frac{(x_c - l_i) \cdot v_{chip}}{2 \cdot a}} \cdot \left[K_0 \cdot \left(\frac{R_i \cdot v_{chip}}{2 \cdot a} \right) + K_0' \cdot \left(\frac{R_i' \cdot v_{chip}}{2 \cdot a} \right) \right] \cdot dl_i \quad (6)$$

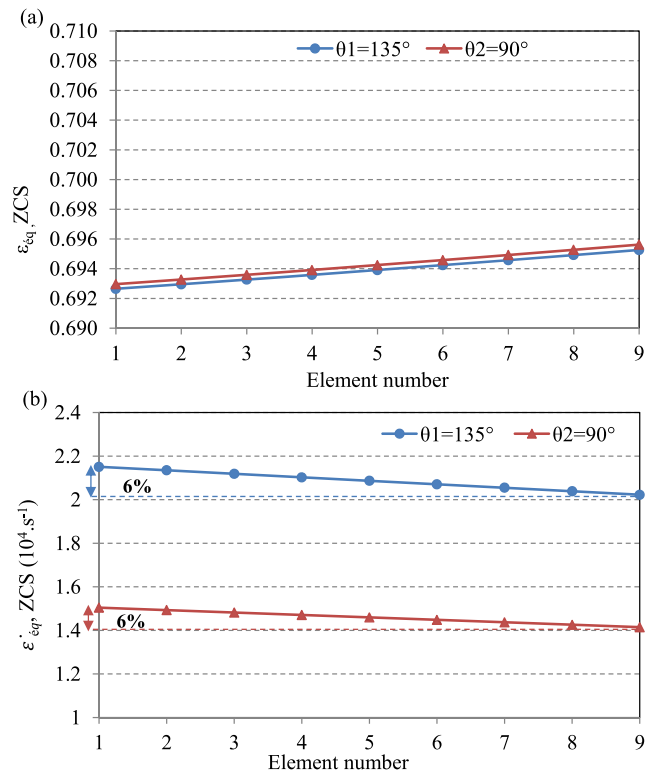


Fig. 7 Variation in **a** strain and **b** strain rate in the SSZ for each element of the edge (tool with straight edge—9 elements)

The graphs in Fig. 8a represent the change in temperature along the cutting edge for each length element. The average temperature in the secondary shear zone increases closer to the tool tip. The temperature gradient decreases moving from position θ_1 towards position θ_2 . This variation is due to greater heat propagation with θ_2 , generated by the increase in the cross-section of the chip when changing from θ_1 to θ_2 .

The force normal to the rake face in the secondary shear zone decreases slightly along the straight cutting edge. This small variation is because the discretization of the depth of cut is constant for all elements.

3.2.2 Study of the rounded part of the edge

For the rounded part of the edge and in order to move closer to a linear distribution of the velocity fields in the different cutting zones [17], the cutting edge is discretized into constant lengths d_{y4} (Fig. 9). This discretization produces elements with different depths of cut a_{pi} .

The strain fields and strain rates are determined by applying Yousfi’s approach [17] to each length element. The graphs in Fig. 10a, b show the change in equivalent strain and overall strain rate along this rounded part of the cutting edge (in the secondary shear zone). For the two angle

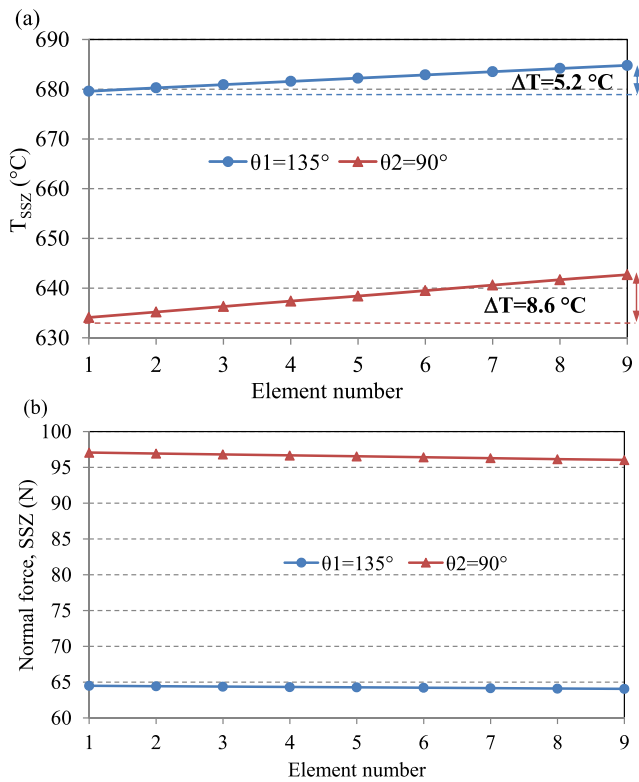


Fig. 8 Variations in **a** average temperature in the SSZ for each element of the edge, and **b** force normal to the rake face

positions θ_1 and θ_2 , equivalent strain increases dramatically when moving closer to the generated surface (Fig. 10a) and

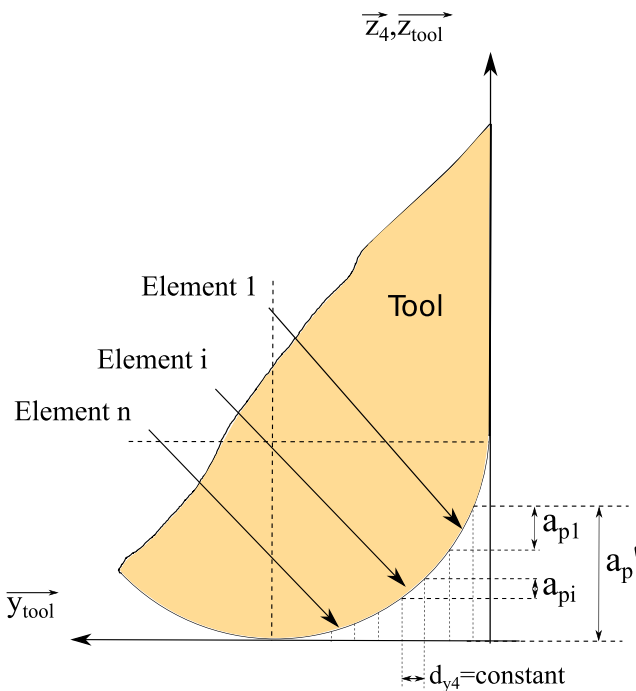


Fig. 9 Discretization of the rounded part of the cutting edge

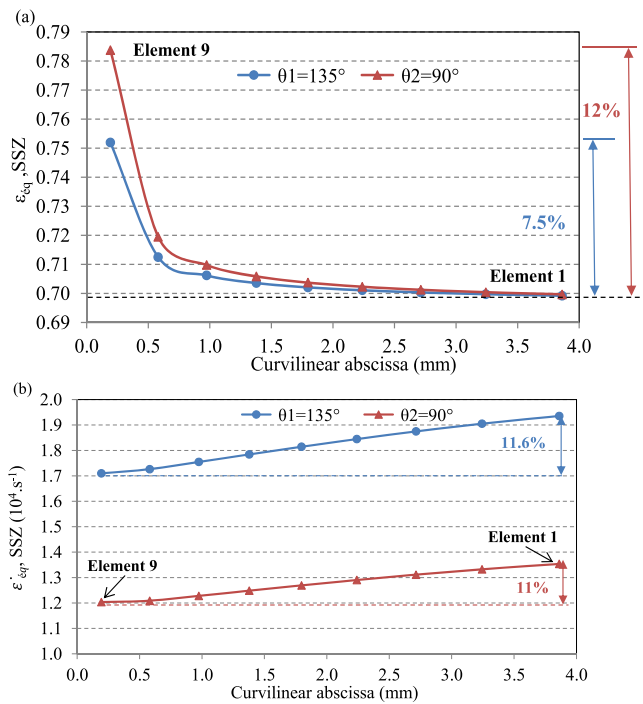


Fig. 10 Variations in **a** strain and **b** strain rate in the SSZ for each element of the edge (rounded tool—9 elements) for $r_e = 4 \text{ mm}$

this change is due to the geometry of the tool. The overall strain rate along the edge decreases, by 11% on average, when moving closer to the machined surface (Fig. 10b).

The graphs in Fig. 11a show the change in average temperature along the cutting edge for each length element. The average temperature in the secondary shear zone increases when moving closer to the generated surface of the workpiece. This temperature gradient is due to the decrease in the cross-section of the chip locally. The temperature gradient decreases from position θ_1 to position θ_2 , generated by the increase in the cross-section of the chip (when moving from θ_1 to θ_2).

The decrease in the cutting edge width a_{pi} from element 1 to element 9 generates a substantial decrease in the force normal to the rake face in the secondary shear zone which tends towards 0. Instantaneous feed is higher in position θ_2 and generates a greater force than that in position θ_1 .

4 Calculation of overall cutting actions and validation of the model

4.1 Calculation of overall cutting actions

The elementary cutting action torsor applied in coordinate system \mathcal{R}_f , defined according to tool orientations κ_r, γ_0 and

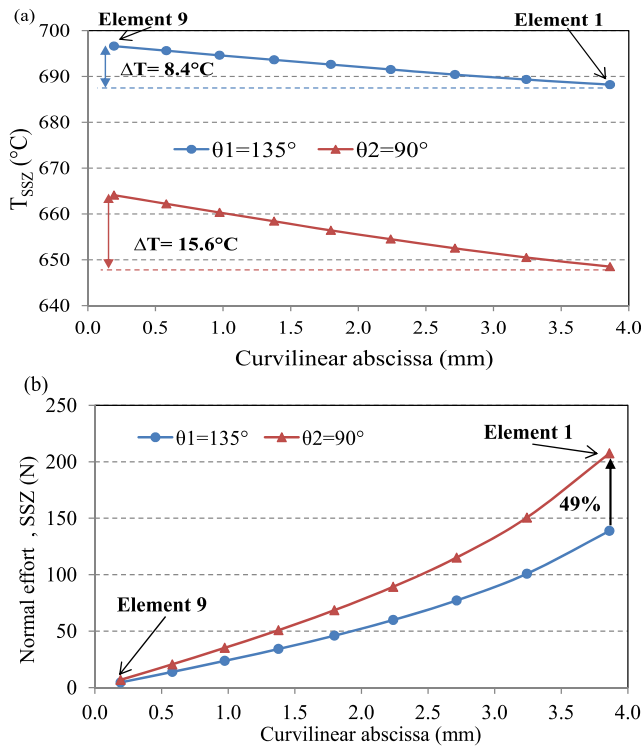


Fig. 11 Variations in **a** average temperature in the SSZ for each element of the edge and **b** force normal to the rake face

λ_s [16], on each length element of the cutting edge takes the form

$$P_i [\tau_{i,W_P \rightarrow T}]_{\mathcal{R}_f} = P_i [\rightarrow R_{W_P \rightarrow T} \rightarrow M_{P_i, W_P \rightarrow T}]_{\mathcal{R}_f} = \begin{bmatrix} F_{c_i, P_i} & 0 \\ F_{t_i, P_i} & 0 \\ F_{z_i, P_i} & 0 \end{bmatrix}_{\mathcal{R}_f}, \quad (7)$$

using, W_P for workpiece and T for tool.

In this study, we consider only local moments generated by the kinematics and the geometry of the tool. Moments generated by the behavior of the material are not dealt with here [22]. Cutting forces and tangential forces in each zone generate local moments which are dependent on the position of each point in relation to the theoretical tool tip. For the linear part of the cutting edge, the overall torsor at the tool tip in coordinate system \mathcal{R}_f equals the sum of the elementary torsors expressed in the same coordinate system, and therefore becomes

$$P [\tau_{W_P \rightarrow T}]_{\mathcal{R}_f} = \begin{bmatrix} F_{cf} \\ F_{tf} \\ F_{zf} \\ M_{xf} \\ M_{yf} \\ M_{zf} \end{bmatrix}_{\mathcal{R}_f}, \quad (8)$$

with

$$P \vec{P}_i = \begin{bmatrix} 0 \\ 0 \\ d_{2iz} \end{bmatrix}_{\mathcal{R}_f}, \quad (9)$$

and where

$$\begin{aligned} F_{cf} &= \sum_{i=1}^n F_{c_i, P_i}, \\ F_{tf} &= \sum_{i=1}^n F_{t_i, P_i}, \\ F_{zf} &= \sum_{i=1}^n F_{z_i, P_i}, \\ M_{xf} &= \sum_{i=1}^n -d_{2iz}(z) \cdot F_{t_i, P_i}, \\ M_{yf} &= \sum_{i=1}^n d_{2iz}(z) \cdot F_{c_i, P_i}, \\ M_{zf} &= 0. \end{aligned} \quad (10)$$

In order to compare the results from analytical modelling with the experimental results, the action torsor must be expressed in the tool’s initial coordinate system (before orientation). After transporting it to this initial coordinate system \mathcal{R}_{ini} , this torsor takes the following form:

$$P [\tau_{W_P \rightarrow T}]_{\mathcal{R}_{ini}} = \begin{bmatrix} F_{c1} \\ F_{t1} \\ F_{z1} \\ M_{x1} \\ M_{y1} \\ M_{z1} \end{bmatrix}_{\mathcal{R}_{ini}}, \quad (11)$$

where

$$\begin{aligned} F_{c1} &= \cos(\lambda_s) \cdot F_{cf} + \sin(\lambda_s) \cdot \cos(\kappa_r) \cdot F_{tf} \\ &\quad + \sin(\lambda_s) \cdot \sin(\kappa_r) \cdot F_{zf}, \\ F_{t1} &= \sin(\kappa_r) \cdot F_{tf} - \cos(\kappa_r) \cdot F_{zf}, \\ F_{z1} &= -\sin(\lambda_s) \cdot F_{cf} + \cos(\lambda_s) \cdot \cos(\kappa_r) \cdot F_{tf} \\ &\quad + \cos(\lambda_s) \cdot \sin(\kappa_r) \cdot F_{zf}, \\ M_{x1} &= \cos(\lambda_s) \cdot M_{xf} + \sin(\lambda_s) \cdot \cos(\kappa_r) \cdot M_{yf}, \\ M_{y1} &= \sin(\kappa_r) \cdot M_{yf}, \\ M_{z1} &= -\sin(\lambda_s) \cdot M_{xf} + \cos(\lambda_s) \cdot \cos(\kappa_r) \cdot M_{yf}. \end{aligned} \quad (12)$$

The same was done for the rounded part of the cutting edge. In this case, the overall action torsor in coordinate

Table 1 Mechanical characteristics of 42CrMo4 and Johnson-Cook parameters

Property	Value
Hardness (Hv)	260
Young’s modulus (GPa)	210
A	598
B	768
C	0.013
m	0.209
n	0.807

Table 2 Cutting conditions

Test no.	$a_p(mm)$	$f_z(mm.tooth^{-1})$	$V_c(m.min^{-1})$
1	1	0.1	50
2	1	0.1	150
3	1	0.2	150
4	2	0.1	150

system \mathcal{R}_f represented at the theoretical tool tip is then

$${}^P[\tau_{WP \rightarrow T}]_{\mathcal{R}_f} = \begin{bmatrix} F_{cf} \\ F_{tf} \\ F_{zf} \\ M_{xf} \\ M_{yf} \\ M_{zf} \end{bmatrix}_{\mathcal{R}_f}, \tag{13}$$

with

$$\vec{P}P_i = \begin{bmatrix} 0 \\ d_{1iy}(y) \\ d_{1iz}(y) \end{bmatrix}_{\mathcal{R}_f}, \tag{14}$$

and where

$$\begin{aligned} F_{cf} &= \sum_{i=1}^n F_{c_i, P_i}, \\ F_{tf} &= \sum_{i=1}^n F_{t_i, P_i}, \\ F_{zf} &= \sum_{i=1}^n F_{z_i, P_i}, \\ M_{xf} &= \sum_{i=1}^n d_{1iy}(y) \cdot F_{z_i, P_i} \cdot \cos(\gamma_0) \\ &\quad - d_{1iz}(y) \cdot F_{t_i, P_i}, \\ M_{yf} &= \sum_{i=1}^n d_{1iz}(y) \cdot F_{c_i, P_i} \\ &\quad - d_{1iy}(y) \cdot F_{z_i, P_i} \cdot \sin(\gamma_0), \\ M_{zf} &= \sum_{i=1}^n d_{1iy}(y) \cdot \sin(\gamma_0) \cdot F_{t_i, P_i} \\ &\quad - d_{1iy}(y) \cdot \cos(\gamma_0) \cdot F_{c_i, P_i}. \end{aligned} \tag{15}$$

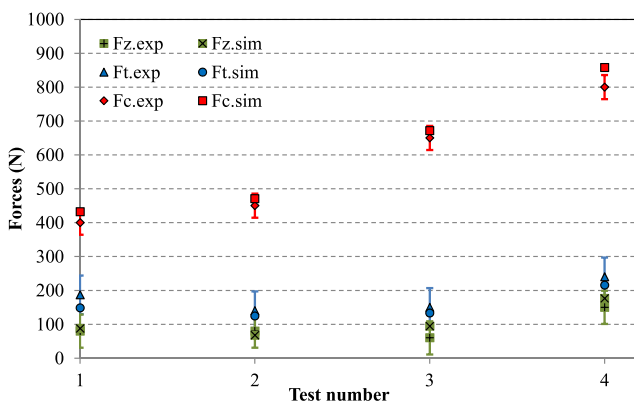


Fig. 12 Comparison of analytical and experimental forces

Table 3 Errors between simulated and experimental forces

Test no.	ΔF_x (%)	ΔF_y (%)	ΔF_z (%)
1	8	-20.6	9.2
2	4.5	-11	-15.1
3	3.3	-11.4	57.2
4	7.2	-10.3	17.5

Transporting the action torsor to coordinate system \mathcal{R}_{ini} gives the following:

$${}^P \begin{bmatrix} F_{c2} \\ F_{t2} \\ F_{z2} \\ M_{x2} \\ M_{y2} \\ M_{z2} \end{bmatrix}_{\mathcal{R}_{ini}} = \begin{bmatrix} \cos(\lambda_s) \cdot F_{cf} + \sin(\lambda_s) \cdot F_{zf} \\ F_{tf} \\ -\sin(\lambda_s) \cdot F_{cf} + \cos(\lambda_s) \cdot F_{zf} \\ \cos(\lambda_s) \cdot M_{xf} + \sin(\lambda_s) \cdot M_{zf} \\ M_{yf} \\ -\sin(\lambda_s) \cdot M_{xf} + \cos(\lambda_s) \cdot M_{zf} \end{bmatrix}_{\mathcal{R}_{ini}}. \tag{16}$$

On each element of the cutting edge, the elementary force component F_{z_i, P_i} is determined by projecting the resulting cutting forces. These are a function of the elementary cutting forces calculated in the elementary cutting plane (perpendicular to the edge) and of a sliding coefficient α_z defined as the ratio of the two respective speeds of the chip V_{cop_i, P_i} and V_{z_i, P_i} and parallel to the cutting edge (17).

$$tg(\alpha_{z_i}) = \frac{V_{z_i, P_i}}{V_{cop_i, P_i}}. \tag{17}$$

4.2 Validation of the model

Results from the theoretical model developed in this study are compared with the results of experimental milling tests by Albert [5] on a square tool of uncoated carbide machining a 42CrMo4 steel (close to AISI 4142 steel) [23]. The Johnson-Cook behavior law (5) parameters for the used material are given in the Table 1. The cutting conditions tested are shown in Table 2. In Albert’s

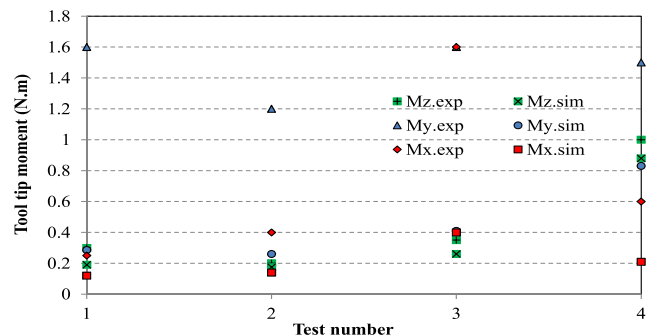


Fig. 13 Comparison of analytical and experimental moments

Table 4 Errors between simulated and experimental moments

Test no.	$\Delta M_{x/O}$ (%)	$\Delta M_{y/O}$ (%)	$\Delta M_{z/O}$ (%)
1	– 52	– 82.1	– 36.6
2	– 48, 15	– 78.3	– 12.5
3	– 75	– 74.3	– 25.7
4	– 65	– 44.6	– 12

work, the dynamometer measurement accuracy at its origin of the dynamometer, point O in a fixed reference, is $\pm 50N$ on forces (F_x , F_y , F_z) and $\pm 4Nm$ on moments ($M_{x/O}$, $M_{y/O}$, $M_{z/O}$).

For a cutting edge angle κ_r of 45° , a rake angle γ_0 of 6° and a cutting edge inclination angle λ_s of 6° , the experimental and simulated cutting forces are shown in Fig. 12.

The comparison of the results from the model and the experimental measurements shows a good correlation of the cutting forces (Table 3), given their level and the scatter dispersion of the measuring apparatus. The deviations in force for component F_t are greater than those for component F_c ; this difference indicates that a more detailed description is needed of the true tribological phenomena at the tool-material interface. Figure 13 shows the components of the moment for the four tests from Table 2.

For the moment components, the comparison between the simulation results and the experimental tests reveals a considerable difference between the two approaches (Table 4). This is due to the fact that only the moments created by the velocity gradient generating the rotation of the chip are taken into account, while the rotation of the material in the shear zones [2] is not considered. Other studies [1] and [22] suggest that new behavior laws may be able to take into account the rotation of the material and the tribological phenomena at the tool-material interfaces. Thus, in this case, the moments identified by this model represent, on average, about 10% of the total cutting power.

5 Conclusion

This work represents a new approach to the calculation of cutting actions (forces and moments) based on calculating strains and strain rates in the main shear zones. The orientation of the tool in space creates strong stress gradients which then directly influence the elementary cutting forces. A considerable variation in strains and strain rates was calculated between the two extreme points of the cutting edge, generating a significant difference between the stress fields. These gradients generate a cutting force gradient between the volume elements and this results in the appearance of a tool tip moment which contributes to total power consumption. The moments determined here are generated by geometry

and kinematics and do not consider the rotation of the material in the cutting zones or the tribological phenomena at the tool-material interfaces. In order to calculate all moments generated during cutting, a new behavior law will need to be developed, which can take into account the rotation of the material in the shear zones and the friction between the material and the tool. This behavior on the part of the material generates significant cutting moments which contribute to the calculation of total power [3].

References

1. Toulouse D, Couétard Y, Cahuc O, Gérard A (1997) An experimental method for the cutting process in three dimensions. In: 5th Conference on mechanical and physical behaviour of materials under dynamic loading, vol C3. Toledo, pp 21–26
2. Laheurte R, Cahuc O, Darnis P, Gérard A (2006) Behaviour law for cutting process. *Int J Adv Manuf Technol En cours de Publ* 29:17–23
3. Cahuc O, Darnis P, Gérard A, Battaglia J-L (2001) Experimental and analytical balance sheet in turning applications. *Int J Adv Manuf Technol* 18(9):648–656. <https://doi.org/10.1007/s001700170025>
4. Dargnat F, Darnis P, Cahuc O (2009) Analytical modelling of cutting phenomena improvements with a view to drilling modelling. *Int J Mach Mach Mater* 5(2):176–206. <https://doi.org/10.1504/ijmmm.2009.02339>
5. Albert G, Laheurte R, K'Nevez J-Y, Darnis P, Cahuc O (2011) Experimental milling moment model in orthogonal cutting condition: to an accurate energy balance. *Int J AdvManuf Technol* 55(9–12):843–854. <https://doi.org/10.1007/s00170-010-3118-0>
6. Battaglia J-L, Puigsegur L, Cahuc O (2005) Estimated temperature on a machined surface using an inverse approach. *Int J Exper Heat Tranfer* 18(1):13–32. <https://doi.org/10.1080/08916150590884826>
7. Zhang X, Ehmann KF, Yu T, Wang W (2016) Cutting forces in micro-end-milling processes. *Int J Mach Tools Manuf* 107(Supplement C):21–40. <https://doi.org/10.1016/j.ijmactools.2016.04.012>
8. Wojciechowski S (2015) The estimation of cutting forces and specific force coefficients during finishing ball end milling of inclined surfaces. *Int J Mach Tools Manuf* 89(Supplement C):110–123. <https://doi.org/10.1016/j.ijmactools.2014.10.006>
9. Wojciechowski S, Maruda RW, Nieslony P, Krolczyk GM (2016) Investigation on the edge forces in ball end milling of inclined surfaces. *Int J Mech Sci* 119(Supplement C):360–369. <https://doi.org/10.1016/j.ijmecsci.2016.10.034>
10. Wojciechowski S, Maruda RW, Barrans S, Nieslony P, Krolczyk GM (2017) Optimisation of machining parameters during ball end milling of hardened steel with various surface inclinations. *Measurement* 111(Supplement C):18–28. <https://doi.org/10.1016/j.measurement.2017.07.020>
11. Karagüzel U, Uysal E, Budak E, Bakkal M (2015) Analytical modeling of turn-milling process geometry, kinematics and mechanics. *Int J Mach Tools Manuf* 91(0):24–33. <https://doi.org/10.1016/j.ijmactools.2014.11.014>
12. Kaymakci M, Kilic ZM, Altintas Y (2012) Unified cutting force model for turning, boring, drilling and milling operations. *Int J Mach Tools Manuf* 34–45:54–55
13. Engin S (2001) Mechanics and dynamics of general milling cutters. Part II: inserted cutters. *Int J Mach Tools Manuf* 41(15):2213–2231. [https://doi.org/10.1016/S0890-6955\(01\)00046-3](https://doi.org/10.1016/S0890-6955(01)00046-3)

14. Kang YH, Zheng CM (2013) Mathematical modelling of chip thickness in micro-end- milling: a fourier modelling. *Appl Math Modell* 37(6):4208–4223. <https://doi.org/10.1016/j.apm.2012.09.011>
15. Zhou L, Peng FY, Yan R, Yao PF, Yang CC, Li B (2015) Analytical modeling and experimental validation of micro end-milling cutting forces considering edge radius and material strengthening effects. *Int J Mach Tools Manuf* 97(Supplement C):29–41. <https://doi.org/10.1016/j.ijmactools.2015.07.001>
16. Yousfi W, Laheurte R, Darnis P, Cahuc O, Calamaz M (2016) 3D modelling of kinematic fields in the cutting area: application to milling. *Int J Adv Manuf Technol* 86:2735–2745. <https://doi.org/10.1007/s00170-016-8396-8>
17. Yousfi W, Darnis P, Cahuc O, Laheurte R, Calamaz M (2015) 3D modeling of strain fields and strain rate in the cutting area: application to milling. *Int J Adv Manuf Technol* 1–12. <https://doi.org/10.1007/s00170-015-7848-x>
18. Oxley PLB (1961) Mechanics of metal cutting. *Int J Mach Tool Des Res* 1(1–2):89–94
19. Marinov VR (2001) Hybrid analytical-numerical solution for the shear angle in orthogonal metal cutting – Part II: experimental verification. *Int J Mech Sci* 43(2):415–426
20. Johnson G, Cook W (1983) A constitutive model and data for metals subjected to large strains, high strain rates and high temperatures. In: *Proceedings of the Seventh international symposium on ballistics*. The Hague, pp 541–547
21. Komanduri R, Hou ZB (2001) Thermal modeling of the metal cutting process—part III: temperature rise distribution due to the combined effects of shear plane heat source and the tool-chip interface frictional heat source. *Int J Mech Sci* 43(1):89–107
22. Royer R, Cahuc O, Gérard A (2011) Strain gradient plasticity applied to material cutting. *Adv Mater Res* 423:103–115. <https://doi.org/10.4028/www.scientific.net/AMR.423.103>
23. Hamann JC, Grolleau V, Le Maître F (1996) Machinability improvement of steels at high cutting speeds—study of tool/work material interaction. *CIRP Ann Manuf Technol* 45(1):87–92. [https://doi.org/10.1016/S0007-8506\(07\)63022-4](https://doi.org/10.1016/S0007-8506(07)63022-4)